High-Temperature Mechanical Properties of Aluminum Alloy Matrix Composites Reinforced with Zr and Ni Trialumnides Synthesized by In Situ Reaction

LIWEN PAN, SAINAN ZHANG, YI YANG, NIKHIL GUPTA, CHAO YANG, YANJUN ZHAO, and ZHILIU HU

High-temperature strengths and stabilities of Al_3Ni and Al_3Zr phases can be used to develop heat-resistant Al-matrix composites. In the current study, Al-1Mg-0.8Mn-0.8V alloy matrix composites are synthesized by in-situ reaction of K_2ZrF_6 salt and Ni powder to yield Al_3Zr- and Al_3Ni-reinforcing phases. The as-cast microstructural and room-temperature and high-temperature tensile properties of the composite are investigated. The microstructure of the composites contain α-Al, Al_3Zr, Al_3Ni, and $Al_{10}V$ phases. The eutectic mixture comprises alternating Al_3Ni and α-Al phases with fine Al_3Zr precipitates distributed in the interlamellar regions. The (2 pct Al_3Zr + 15.2 pct Al_3Ni)/Al-alloy composite shows the highest mechanical properties at room temperature, with a tensile strength of 198 MPa and a fracture strain of 6.55 pct. At 200 and 300 °C, tensile strengths of (2 pct Al_3Zr + 13.3 pct Al_3Ni)/Al-alloy and (2 pct Al_3Zr + 15.2 pct Al_3Ni)/Al-alloy composites reach 175 MPa and 166 MPa, and 191 MPa and 155 MPa, respectively. At 350 °C, the highest tensile strength of this composite family reaches 82 MPa, which surpasses some of the existing Al-Si alloys used in automotive pistons, suggesting its potential high-temperature applications. Analysis indicates that the fracture mode of the present composites is ductile. Transgranular cleavage fracture of coarse, brittle $Al_{10}V$ phase, and microvoid coalescence are the main failure mechanisms.

https://doi.org/10.1007/s11661-019-05511-7

I. INTRODUCTION

THE high-temperature mechanical properties of conventional aluminum alloys are unable to meet the requirements of mechanical properties of new automotive engines that work at temperatures above 300 °C.[1] At such high temperatures, coarsening or dissolution of the strengthening phases at elevated temperature results in loss of mechanical properties of the alloy and make them unsuitable for engine applications.[1] Aluminum matrix composites have been studied as promising materials for such applications.[2,3] In-situ aluminum matrix composites have been investigated and have shown promising tensile and wear properties for such applications[4] but their high-temperature properties are not determined. The α-Al matrix of these alloys is mainly strengthened by eutectic mixture and intermetallic phases such as Al_2Cu and Mg_2Si, depending on the alloy composition. However, spheroidization of Si particles may reduce the high-temperature strength of Al-Si alloys.[5] The Al_2Cu and Mg_2Si intermetallic phases are effective in improving strength and creep resistance of the alloys at elevated temperatures but only below 200 °C.[6,7] Many cast Al-Si alloys have hypereutectic composition and contain coarse, angular primary silicon phase, resulting in low strength and ductility of the alloys.[8] Casting defects such as porosity and inclusions are observed in cast Al-Si alloys due to a broad "mushy zone". These defects considerably degrade the mechanical properties and service life of the alloys.[8] Therefore, it is desired to develop new high-temperature alloys as substitutes to the conventional Al-Si alloys.

LIWEN PAN and ZHILIU HU are with the Guangxi Key Laboratory of Processing for Non-ferrous Metal and Featured Materials, School of Resources, Environment and Materials, Guangxi University, Nanning 530004, P.R. China and also with the Center Ecological Collaborative Innovation for Aluminum Industry in Guangxi, Nanning 530004, P.R. China. SAINAN ZHANG, CHAO YANG, and YANJUN ZHAO are with the Guangxi Key Laboratory of Processing for Non-ferrous Metal and Featured Materials, School of Resources, Environment and Materials, Guangxi University. YI YANG and NIKHIL GUPTA are with the Composite Materials and Mechanics Laboratory, Department of Mechanical and Aerospace Engineering, Tandon School of Engineering, New York University, Brooklyn, NY 11201. Contact e-mail: ngupta@nyu.edu
Manuscript submitted July 28, 2019.
Article published online November 1, 2019

Studies have attempted to introduce thermally stable trialuminides by microalloying of transition metals (TM) to improve elevated-temperature mechanical properties of aluminum alloys.[1,9–11] Precipitation strengthening was provided by Al_3Zr and Al_3Ni by adding Zr and Ni, respectively, in aluminum alloys is found to be promising in this regard. Al_3Zr serves as a high-temperature strengthening phase due to its high melting point (1580 °C), high modulus of elasticity (205 GPa), high thermal stability (425 °C),[12] slow diffusivity in Al-matrix (at 400 °C, $D_{Zr} = 1.2 \times 10^{-20}$ m^2/s[13]) and low interfacial free energy with α-Al.[14,15] However, the strengthening effect of Al_3Zr in aluminum alloys is significantly limited due to its low solid solubility (the solubility limit of Zr in α-Al, $C_{\alpha p\text{-}Zr} \cong 0.28$ wt pct[13]), which limits its ability to provide strengthening effect.[11] Adding an excess amount of Zr into aluminum melt causes precipitation of primary Al_3Zr by peritectic reaction during solidification. Although these primary Al_3Zr precipitates can be conducive to improving the elevated-temperature mechanical properties, the equilibrium form of Zr trialuminides that form by a peritectic reaction is often coarse and incoherent with the α-Al matrix, and adds little strength to the alloy.[16] Increasing the quantity of these precipitates is detrimental to room-temperature properties due to their low crystal symmetry.[17,18]

The eutectic reaction of Ni and Al can generate high-temperature (> 500 °C) stable Al_3Ni intermetallic phase[19] to obtain high-temperature stability in the composite. Morphology of the Al-Al_3Ni eutectic mixture significantly influences the mechanical properties of the composite.[20] Addition of Ni to Al-Si-Cu-Mg alloy produces strengthening phases such as Al_3Ni, Al_3CuNi, and Al_7Cu_4Ni. The tensile strength of the alloy at high temperature (350 °C) can reach 62 MPa because of Al_3CuNi phase[21] and adjustment of Cu content can further improve the high-temperature strength at 350 °C to 93.5 MPa.[22] Conventional Al-Si and Al-Si-Cu system have been studied for increasing their thermal stability with Al_3Ni but the presence of low thermal stability phases Mg_2Si and Al_2Cu limit their advantage.

Mg, Mn, and V are common alloying elements in Al-alloys. Mg increases the strength, hardness, and corrosion resistance of Al alloys but at the expense of ductility and impact resistance.[23] However, Mg addition is limited to small amounts because it may cause hot brittleness and reduce the castability. The strength of Al-alloys increases with Mn content without a loss in ductility up to 0.8 wt pct. The addition of Mn to commercial 6000, 7000, and 8000 series Al-alloys significantly increases the strength without loss of ductility.[24] Studies suggest that V could serve as a grain refiner in Al-alloys[25] likely because V promotes heterogeneous nucleation during solidification.[26] Moreover, it is observed that the presence of Zr in V containing Al-alloys can lead to precipitation of fine $Al_3(Zr_x, V_{1-x})$ phase after heat treatment, which has significantly higher thermal stability than Al_3Zr and Al_3V caused by their low lattice mismatch with the aluminum matrix.[13]

The current study is focused on synthesizing Al-Mg-Mn-V alloy (without Si and Cu) matrix in-situ composites containing Al_3Zr and Al_3Ni precipitates by direct melt reaction (DMR) method in order to obtain high volume fraction of strengthening phases with the desired microstructure. These phases are expected to provide high-temperature stability and strengthening effect in the composite. The in-situ reaction methods of composite synthesis, such as DMR, have many advantages, such as the volume fraction of the reinforcing phase can be varied over a wide range, and a clean interface between the strengthening phase and the matrix can be obtained without having to separately addressing the issue of wettability. Particularly, the DMR method is known for its simplicity, low cost, and near-net-shape-forming capabilities.[27] DMR method has been used with success to introduce Al_3Zr trialuminide in Al matrix by adding K_2ZrF_6 inorganic salt.[27–30] However, the available studies have not focused on understanding the high-temperature characteristics, especially the microstructural and mechanical properties and retention of mechanical properties above the intended use temperature of 300 °C. The as-cast microstructural, room-temperature, and elevated-temperature mechanical properties of the composite are studied, which lay the foundation for developing new varieties of heat-resistant aluminum matrix composites.

II. MATERIALS AND PROCEDURES

The ($x$$Al_3Zr$ + $y$$Al_3Ni$)/Al-1Mg-0.8Mn-0.8V ($x$ and y represent wt pct) composites were synthesized in a mid-frequency induction furnace (20~40 kHz) by using Al, Mg plate, and powders of Ni, Mn, and V, all of which are 99.9 pct pure as well as analytically pure inorganic salt K_2ZrF_6. First, aluminum ingots were melted in a graphite crucible. Covering agent (50 pct NaCl + 50 pct KCl, powder) was added to the melt surface. The temperature of the melt is controlled at 720 °C and held for 5 minutes. The melt temperature was measured using a metallic thermocouple with a digital indicator dipped into the melt and was controlled by adjusting the power. Then, the melt was deslagged and then mechanically stirred at 600 r/min. Ni, V, Mn, Mg, Al-5Ti-1B refining agent, and K_2ZrF_6 salt were added successively while stirring. This process lasts for about 10 minutes. C_2Cl_6 refining agent was added after stirring and then the melt was allowed to sit for 5 minutes. Finally, the melt was deslagged again and poured into a preheated (100~150 °C) permanent cylindrical die (20 mm inner diameter and 135 mm height).

Specimens of 10 mm diameter and 10 mm length were cut by a CNC wire cutting machine for microscopy. A TD-2500 X-ray diffractometer was used for composition analysis. The K_α radiation of Cu target, 20 mA current, 6°/min scanning speed, and 15° to 85° scanning angle range were selected as the scanning parameters. The microstructures and chemical compositions were analyzed by the Phenom scanning electron microscope/energy dispersive spectrometer (SEM/EDS). Room-temperature and high-temperature (200 °C, 300 °C, and

350 °C) tensile tests were conducted on a WDW3100 computer controlled universal testing machine at cross-head displacement speed of 0.5 mm/min. Specimens for high-temperature tests were homogenized at the set temperatures for 20 minutes before loading. Figure 1 shows the size of the cylindrical specimens used for the tensile test. The surfaces of the tensile specimens were polished before testing.

III. RESULTS AND DISCUSSION

A. *Effect of Al_3Zr Content Variation*

1. *Microstructure*

Figure 2 shows XRD patterns of the as-cast ($x$$Al_3Zr$ + 11.7 pct Al_3Ni)/Al-1Mg-0.8Mn-0.8V composites with different mass fraction of Al_3Zr (x = 1, 2, 3 and 4 pct). The results show that the microstructures of four composites mainly consist of α-Al, Al_3Ni, Al_3Zr, and $Al_{10}V$ as well as a small amount of Al_3Ti phase.

Figure 3 depicts the locations of EDS analysis conducted on the microstructure, and the corresponding results are presented in Table I for 2 pct Al_3Zr composite. It can be observed that some Mg, Mn, and V elements are dissolved in the Al_3Ni phase, while Mg, V, Ni, and Ti elements are found dissolved in the Al_3Zr phase. Figure 4 shows that the composite matrix is composed of dark α-Al dendrites, and the Al-Al_3Ni eutectic mixture is distributed in the interdendritic regions. This distribution should be related to the Ni content. Mass fraction of Al_3Ni is 11.7 pct, and the corresponding Ni addition level is 5 wt pct, which is lower than the Al-Ni equilibrium eutectic composition (6.1 pct Ni[13]). The hypoeutectic Al-Ni alloy contains primary α-Al dendrites precipitate followed by precipitation of Al-Al_3Ni eutectic mixture in the interdendritic region. The platelet-like morphology of Al_3Ni phase, appearing as closely spaced lines in the cross-section micrographs, is similar to the previous observations.[19,31–34] Moreover, very fine particles of Al_3Zr (≈ 1 to 5 μm) are distributed between the Al_3Ni platelets. A small amount of coarse, blocky $Al_{10}V$ phase is also observed in the matrix, which indicates that the V content (0.8 wt pct) is slightly over the solubility limit of V in α-Al ($C_{\alpha p\text{-}V} \cong 0.56$ wt pct.[13]

As the mass fraction of Al_3Zr changes, the shapes and sizes of the primary α-Al phase and the relative amount of α-Al + Al_3Ni eutectic mixture are also changed, as observed in Figure 4. With the increasing Al_3Zr content, the size and amount of the primary α-Al dendrites are reduced. The relative amount of Al + Al_3Ni eutectic mixture increases with the increasing Al_3Zr. It is likely that the reduction of the primary α-Al dendrites and the

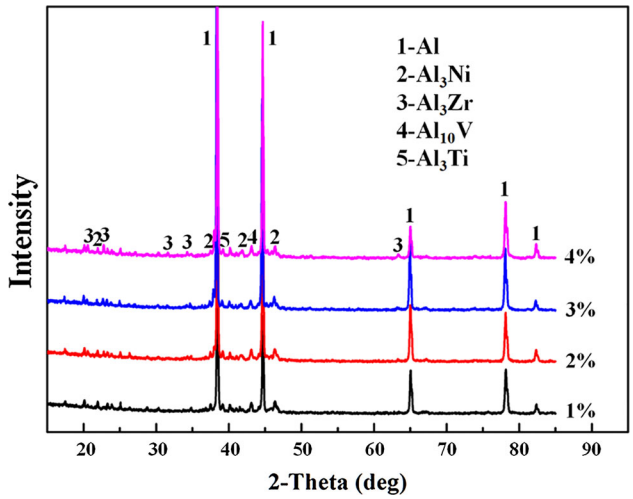

Fig. 2—XRD pattern of ($x$$Al_3Zr$ + 11.7 pct Al_3Ni)/Al-1Mg-0.8Mn-0.8V composites with different mass fractions of Al_3Zr.

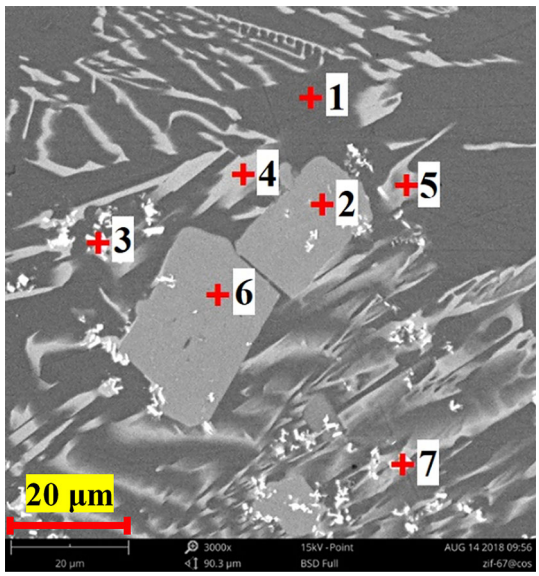

Fig. 3—EDS spot scanning regions of composite (2 pct Al_3Zr + 11.7 pct Al_3Ni) /Al-1Mg-0.8Mn-0.8V.

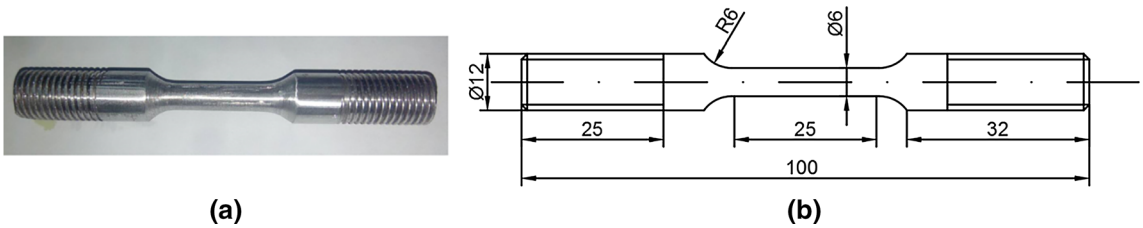

Fig. 1—(*a*) Photo and (*b*) dimensions of the tensile specimen.

increase of Al + Al_3Ni eutectic structure are related to the addition of K_2ZrF_6 that reacted with aluminum melt and consumed Al. The reaction of Al and K_2ZrF_6 occurs at over 700 °C, while Al-Ni eutectic reaction temperature is 640 °C.[13] The relative concentration of Ni in the melt is closer to eutectic composition (6.1 Ni wt pct) when the melt temperature is below 640 °C, which results in a higher amount of Al + Al_3Ni eutectic mixture, as shown in Figures 4(c) and (d). The fine particles of Al_3Zr appear to be aggregated, and the segregation seems to increase with the increasing Al_3Zr content, which indicates that these particles are difficult to disperse uniformly, even with applied mechanical stirring.

2. *Room-temperature mechanical properties*

Figure 5 shows the room-temperature engineering stress–strain curves of ($x$$Al_3Zr$ + 11.7 pct Al_3Ni)/Al-1Mg-0.8Mn-0.8V composites containing various Al_3Zr mass fractions. The tensile properties measured from these tests are given in Table II. The tensile strength and yield strength of the composite with 1 and 2 pct Al_3Zr are higher than other compositions, and the tensile strength of 2 pct Al_3Zr is close to 190 MPa.

When the mass fraction of Al_3Zr increases to 3 and 4 pct, the tensile strength of the composites decreases to about 150 MPa, and the yield strength decreases to about 70 MPa. The strengthening effect of Al_3Zr on the mechanical properties of the composite does not follow a linear trend with respect to the Al_3Zr content. Initially high elastic modulus, high strength and fine particle size (average size $\approx$ 1 to 5 μm) of Al_3Zr phase help in obtaining precipitation hardening effects but agglomeration of the precipitated phase start to dominate over 3 wt pct reinforcement (Figures 4(c) and (d)) and leads to decrease in the properties. The (2 pct Al_3Zr + 11.7 pct Al_3Ni)/Al-1Mg-0.8Mn-0.8V composite with a tensile strength of 189 MPa and a fracture strain of 3.29 pct has the best combination of mechanical properties. Although the best room-temperature tensile strength of the present composites is still below 200 MPa, it reaches the room-temperature strength level of some cast MAHLE aluminum piston alloys,[35] such as M126 (180 to 220 MPa), M138 (180 to 220 MPa), and M244 (170 to 210 MPa). The fracture strain of all composites is over 2 pct, which is higher than the above-mentioned MAHLE Al-Si piston alloys ($\approx$ 1 pct).[35]

B. *Effect of Al_3Ni Content Variation*

1. *Microstructure*

The microstructural and mechanical properties of (2 pct Al_3Zr + $x$$Al_3Ni$)/Al-1Mg-0.8Mn-0.8V composites with the Al_3Ni mass fractions of 2.3, 7, 13.3, and 15.2 pct are discussed in this section. Figures 6 and 7 show the XRD patterns and microstructures of the composites. The XRD results show that the microstructure of these alloys is mainly composed of α-Al, Al_3Ni phase, Al_3Zr phase, and a small amount of $Al_{10}V$ phase. It is observed in Figure 7 that Al_3Zr fine particles are bright white and granular, and $Al_{10}V$ phase is larger and blocky. With the increasing Ni addition level and Al_3Ni content, the morphologies of the eutectic structure (α-Al + Al_3Ni) and α-Al phase changed dramatically. When the content of Ni is 1 wt pct, only a small quantity of (Al + Al_3Ni)-divorced eutectic structure is generated and distributed in α-Al interdendritic regions.

The primary α-Al phase is coarse with the average size of about 80 μm. At the Ni content of 3 wt pct, the average dendrite size of α-Al decreases to about 50 μm, while a greater amount of (Al + Al_3Ni) eutectic mixture appears and begins to surround the primary α-Al phase as shown in Figure 7(b). When the Ni content is 5.7 wt pct, only a small amount of primary α-Al dendrites can be observed, while the amount of (Al + Al_3Ni) eutectic mixture is further increased as shown in Figure 7(c). When the Ni content is further increased to 6.5 wt pct, the microstructure is mainly composed of some fine primary Al_3Ni and a significant amount of fine (Al + Al_3Ni) eutectic mixture as well as Al_3Zr particles as shown in Figure 7(d). It appears that the (Al + Al_3Ni) eutectic mixture in Figure 7(d) is finer than that observed in Figures 7(b) and (c). The primary α-Al dendrites are not observed in Figure 7(d).

2. *Tensile properties*

Figure 8 shows the engineering stress–strain curves for (2 pct Al_3Zr + $x$$Al_3Ni$)/Al-1Mg-0.8Mn-0.8V composite with different Al_3Ni mass fractions at room temperature. The corresponding tensile properties are presented in Table III. It can be observed that the tensile strength and yield strength increase with the increase of Ni content (*i.e.*, the increase of Al_3Ni). The tensile strength of the composite with 2.3 wt pct Al_3Ni is measured to be 114 MPa but increases with further addition of Al_3Ni. At 13.3 wt pct of Al_3Ni in the composite (*i.e.*, Ni level becomes close to the Al-Ni eutectic composition), the tensile strength is over 190 MPa and the yield strength reaches 87 MPa. When Al_3Ni content is 15.2 wt pct (*i.e.*, 6.5 wt pct Ni, which is a hypereutectic composition), the tensile strength reaches the highest level of 198 MPa. These observations indicate that having Ni content close to or greater than the Al-Ni eutectic composition is beneficial for mechanical properties of the composite.

C. *High-Temperature Tensile Properties*

Room-temperature test results revealed that the mechanical properties of (2 pct Al_3Zr + $x$$Al_3Ni$)/Al-alloy composites containing 13.3 and 15.2 wt pct of Al_3Ni are high. Here, these compositions are selected for studying their elevated temperature mechanical properties. The high-temperature stress–strain curves for two composites at 200 °C, 300 °C and 350 °C are shown in Figure 9. Table IV presents the corresponding tensile property values.

It is observed that the tensile strength decreases with the increasing temperature, but the decrease is small up to 300 °C, which is attributed to thermal stabilities of Al_3Zr and Al_3Ni phases within this temperature range. The highest tensile strengths at 200 °C and 300 °C are 191 (15.2 wt pct Al_3Ni) and 166 (13.3 wt pct Al_3Ni) MPa, respectively. Tensile strengths at 350 °C are

Table I. EDS Component Analysis of Each Phase (Atomic Percent)

Spot Number*	Al	Mg	Mn	V	Ni	Zr	Ti	Phase Types
1	97.27	1.55	0.36	0.26	0.43	0.00	0.13	α-Al
2	87.42	0.96	4.78	4.61	1.97	0.00	0.25	$Al_{10}V$
3	80.84	0.89	0.00	0.84	1.30	15.73	0.42	Al_3Zr
4	87.02	1.37	0.45	0.24	10.92	0.00	0.00	Al_3Ni
5	88.83	1.20	0.53	0.30	9.14	0.00	0.00	Al_3Ni
6	86.65	0.86	3.61	6.84	1.93	0.00	0.11	$Al_{10}V$
7	79.20	0.90	0.00	0.60	0.82	18.17	0.31	Al_3Zr

Spot numbers 1 to 7 represent the EDS spot scan at corresponding locations shown in Fig. 3.

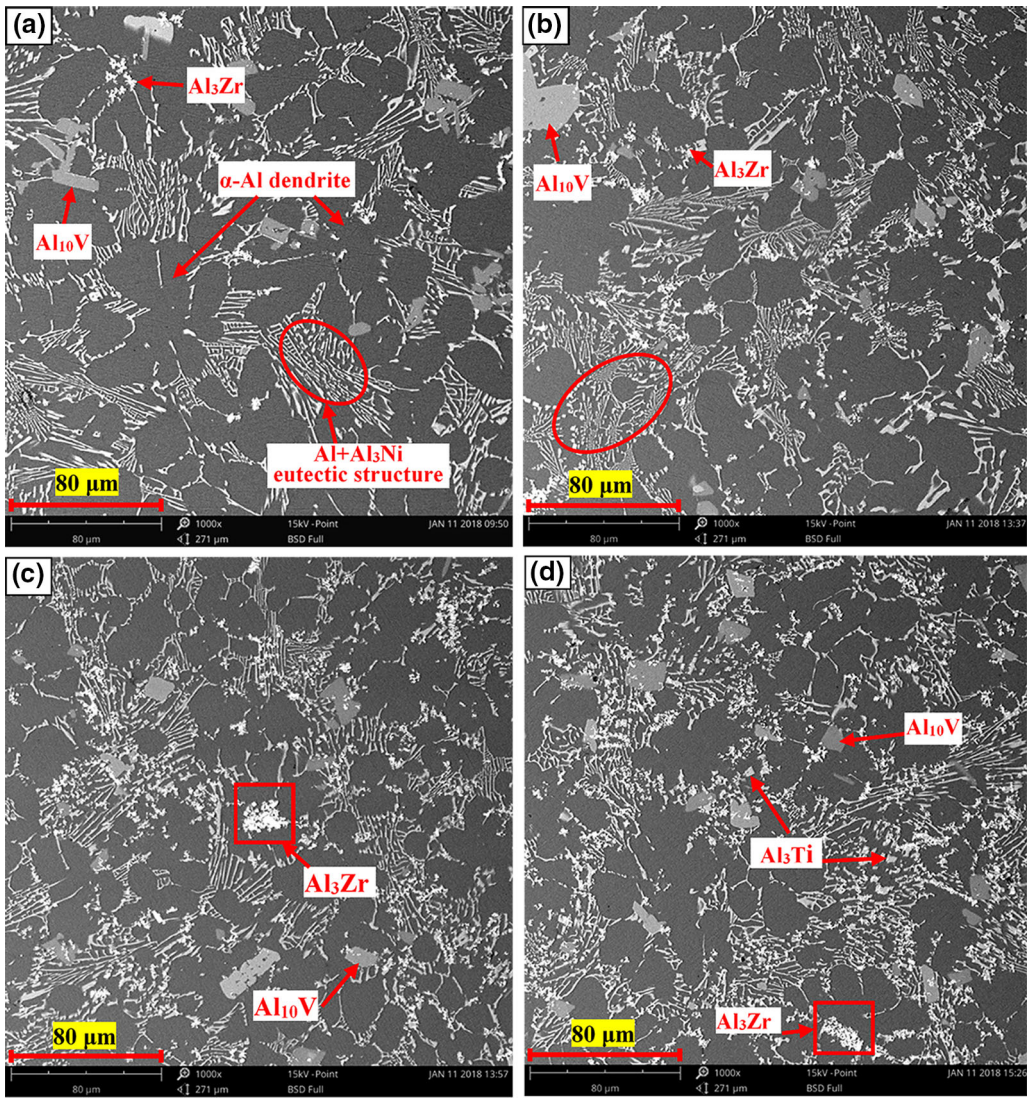

Fig. 4—Microstructures of (xAl_3Zr + 11.7 pct Al_3Ni)/Al-1Mg-0.8Mn-0.8V composites with different Al_3Zr mass fraction: (*a*) x = 1 pct, (*b*) x = 2 pct, (*c*) x = 3 pct, and (*d*) x = 4 pct.

70 MPa (13.3 wt pct Al_3Ni) and 82 MPa (15.2 wt pct Al_3Ni), respectively. In general, the tensile strength values of these two compositions are close to each other. The fracture strain of the composite with 13.3 wt pct Al_3Ni is 8 pct, and that of the composite with 15.2 wt pct Al_3Ni is 6 pct, which are similar to the fracture strains of some MAHLE Al-Si piston alloys.[35] Elevated temperature tensile strengths of these two composites at 350 °C are better than some other Al-Si heat-resistant aluminum alloys as shown in Table V, which suggests their potential application at above 300 °C in the automobile engine field.

The MAHLE aluminum piston alloys such as M124, M126, M138, M142, M145, M174+, and M244 have been widely applied in engines. The comparison data show that the present composites have higher tensile properties and are promising in the high-temperature applications. However, fatigue strength, Young's modulus, thermal conductivity, thermal expansion, and relative wear rate are among other properties that need to be characterized for the present alloy system to ensure they can replace some of the MAHLE alloys in high-temperature applications. The results obtained from the present experiments provide great confidence to conduct these further studies.

D. *Strengthening and Failure Mechanisms*

In dispersion-strengthening mechanism, the matrix is the main load-bearing phase. Rigid particles (usually 1 to 100 nm diameter) hinder the motion of dislocations in the matrix by increasing resistance for dislocation slip, which improves the strength of the composite.[40] However, the average size of most Al_3Zr particles and some Al_3Ni particles is over 1 μm in the present composites. Controlling the size of Al_3Zr and Al_3Ni precipitates by applying mechanical stirring (up to 600 r/min) to the melt during in-situ reaction process was considered. However, very little effect of stirring on the precipitate size was observed at these speeds, and nanoscale Al_3Zr and Al_3Ni precipitates were not formed. Other means such as heat treatments can be explored in the future to reduce the precipitate size to benefit from the strengthening mechanisms that contribute at nanoscale. The larger size (1 to 100 μm diameter) reinforcing precipitates obtained in the current study contribute to a particle strengthening mechanism, where matrix and particles share the load. These particles restrain deformation of the matrix besides hindering the dislocation motion. The platelet-like eutectic phase also contributes to strengthening in these composites. The matrix is not the main load-bearing phase but contributes to transferring the load through the interface, while the Al_3Ni platelets bear the load and strengthen the material. Figures 7(c) and (d) show the presence of Al_3Ni platelet phase in the eutectic mixture. These hard load-bearing platelets contribute to the strengthening of the composite. These two-dimensional platelets are better load bearers compared to the fine particulates present in the microstructure. However, the tensile strengths of the present composites at room and high temperatures are not obviously better than some conventional Al-Si alloys. Random orientation of $Al + Al_3Ni$ eutectic mixture in the matrix due to nondirectional solidification of the alloy is the likely reason that the presence of Al_3Ni has not resulted in increasing the strength compared to that of the conventional Al-Si alloy. Directional solidification may align the eutectic mixture preferentially and provide further improvement in the strength in the direction of lamella. Moreover, there are

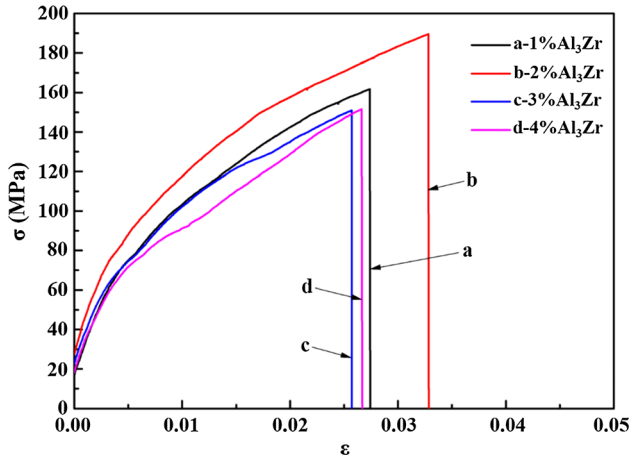

Fig. 5—Tensile stress–strain curves of (xAl_3Zr + 11.7 pct Al_3Ni) / Al-1Mg-0.8Mn-0.8V composite with different Al_3Zr mass fraction.

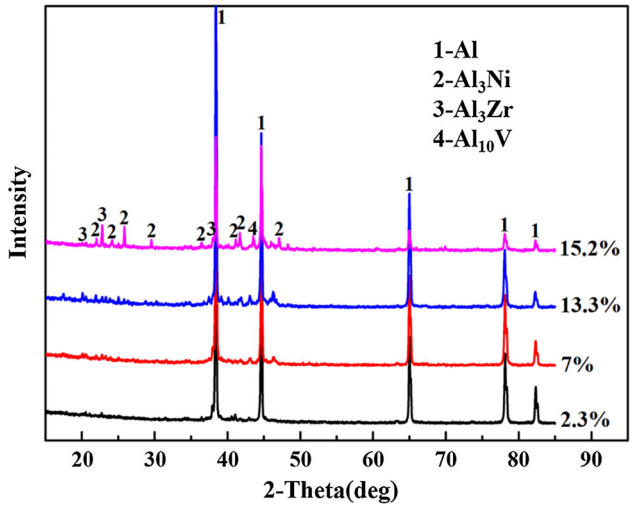

Fig. 6—XRD pattern of (2 pct Al_3Zr + xAl_3Ni)/Al-1Mg-0.8Mn-0.8V composites with different Al3Ni mass fractions.

Table II. Tensile Properties of (xAl_3Zr + 11.7 pct Al_3Ni)/Al-1Mg-0.8Mn-0.8V Composites with Different Al_3Zr Mass Fraction

Mass Fraction of Al_3Zr (Pct)	UTS (σ_b) (MPa)	YS ($\sigma_{0.2}$) (MPa)	Fracture Strain (Pct)	Elongation
1	162	74	2.74	2.04
2	189	80	3.29	2.98
3	151	70	2.57	1.80
4	150	71	2.66	2.23

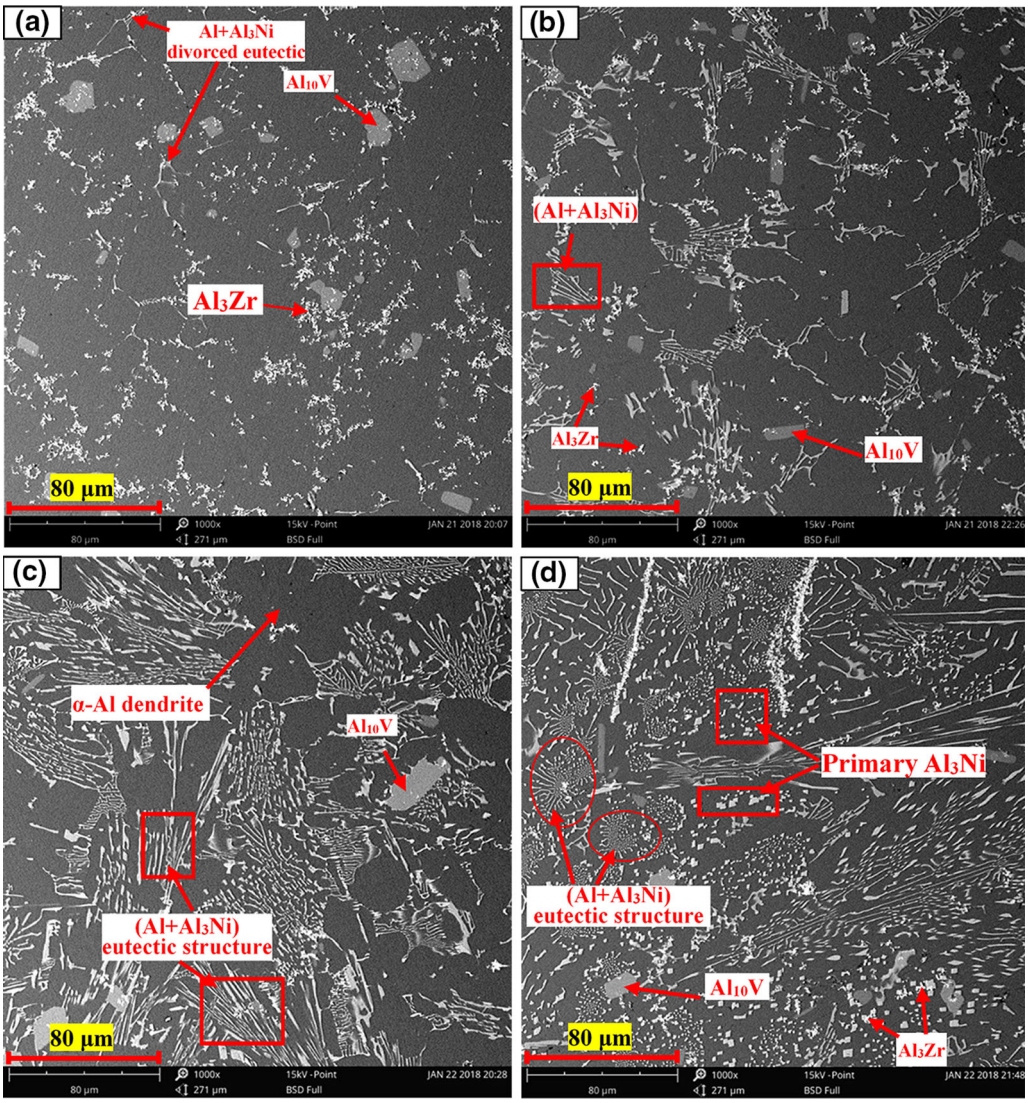

Fig. 7—Microstructure of the composite with different Al_3Ni contents by weight: (*a*) 2.3 pct, (*b*) 7 pct, (*c*) 13.3 pct, and (*d*) 15.2 pct.

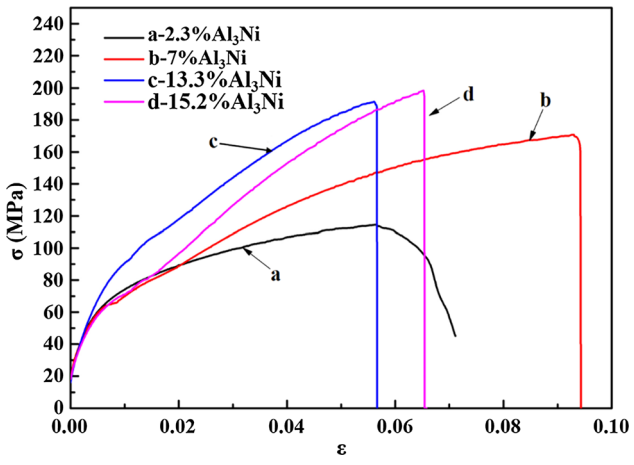

Fig. 8—Tensile engineering stress–strain curves of (2 pct Al_3Zr + xAl_3Ni)/Al-1Mg-0.8Mn-0.8V composites with different Al_3Ni at room temperature.

crystallographic orientation relationship $[\bar{2}\bar{2}1]_{Al3Zr}//[100]_{Al}$, $(012)_{Al3Zr}//(1\bar{1}0)_{Al}$[41] between Al_3Zr and Al matrixes and $(100)_{Al3Ni}\|(\bar{1}31)_{Al}$,$[010]_{Al3Ni}\|[101]_{Al}$[42] between Al_3Ni and Al matrixes, which indicates Al_3Zr and Al_3Ni have coherent relation with the matrix. These orientation relationships provide the phase boundary with strong interface bonding that ensures that decohesion cannot happen at high temperature. Ni has a very low solid solubility limit in the α-Al matrix at room temperature (only 0.05 wt pct[20]) and may not be able to play an important role in strengthening the alloy. Therefore, the particle-reinforced, fiber-reinforced, and coherent strengthening are likely the most important high-temperature strengthening mechanisms in the present composites.

The composite (2 pct Al_3Zr + 15.2 pct Al_3Ni)/ Al-alloy is chosen for failure analysis. Figure 10 shows the failure characteristics of the specimens that were subjected to testing at different temperatures. In all cases,

Table III. Tensile Properties of Composite (2 pct Al_3Zr + xAl_3Ni)/Al-1Mg-0.8Mn-0.8V at Room Temperature

Mass Fraction of Ni Addition (Pct)	Mass Fraction of Al_3Ni (Pct)	UTS (σ_b) (MPa)	YS ($\sigma_{0.2}$) (MPa)	Fracture Strain (Pct)	Elongation (Pct)
1	2.3	114	69	>7.11	5.02
3	7	170	63	9.43	6.52
5.7	13.3	191	87	5.67	3.98
6.5	15.2	198	70	6.55	3.86

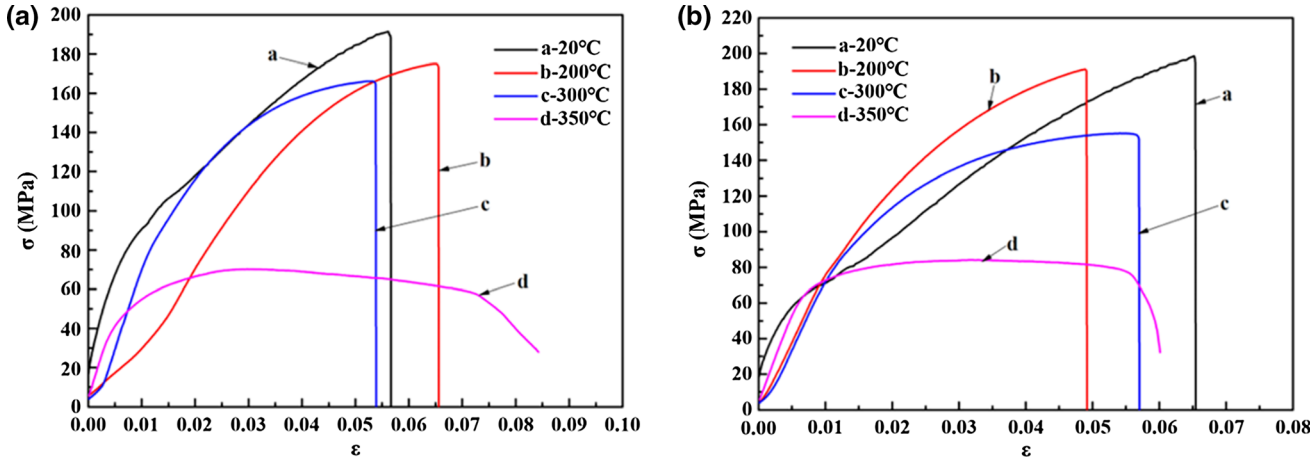

Fig. 9—Tensile stress–strain curves of composites (2 pct Al_3Zr + xAl_3Ni)/Al-1Mg-0.8Mn-0.8V at high temperature: (*a*) x = 13.3 pct and (*b*) x = 15.2 pct.

Table IV. Tensile Properties of Composites (2 Pct Al_3Zr + x Pct Al_3Ni)/Al-1Mg-0.8Mn-0.8V at High Temperature

	UTS (σ_b) (MPa)		YS ($\sigma_{0.2}$) (MPa)		Fracture Strain (Pct)		Elongation (Pct)	
Temperature (°C)	x = 13.3	x = 15.2	x = 13.3	x = 15.2	x = 13.3	x = 15.2	x = 13.3	x = 15.2
25	191	198	87	65	5.67	6.55	3.98	3.86
200	175	191	100	83	6.55	4.92	4.68	3.12
300	166	155	90	85	5.39	5.70	3.75	3.66
350	70	82	48	70	>8.43	6.01	5.24	5.46

the failure shows strong indication of being ductile failure due to the presence of dimples (elliptic regions are equiaxial dimples, rectangular regions are longilineal dimples) created by plastic deformation and microvoid coalescence (MVC). The ductile fracture mode is consistent with the fracture strain values shown in Table IV, which are greater than 5 pct for the composites. This ductile fracture mode is different from the brittle fracture in Al_3Ni and interfacial debonding in Ni-7050 composites reported by earlier studies.[43] Close examination of the fracture surface shows some fine Al_3Zr and Al_3Ni particles in the middle of the equiaxed dimples (Figure 10e), where finer particles lead to smaller dimples. Eutectic Al_3Ni platelets are observed in the center of the elongated dimples (Figure 10f). Al_3Ni platelets separated from the α-Al matrix or fractured into pieces do not appear on the fracture surface, which indicates that there no interfacial debonding or brittle fracture of Al_3Ni. These observations show that the dimples initiate by α-Al matrix plastic deformation around hard Al_3Zr or Al_3Ni precipitates and coalescence of such voids generating larger cracks on the fracture surface. Failure at the interface between these particles and matrix due to stiffness mismatch can also lead to microvoid formation but such separation is not observed in the micrographs. Moreover, the dimples increase in size and number with the increasing testing temperature. Reduction in the interfacial bonding force and softening of the matrix with the increasing temperature also indicate that the interface plays an important role in the failure of these composites.

The fracture surfaces contain some coarse cleavage planes (triangular regions in Figure 10). According to the EDS analysis shown in Figure 11, these blocky phases are $Al_{10}V$, which is a brittle phase with low crystal symmetry that is detrimental to the strength and

Table V. Comparison of Tensile Strength at 350 °C with Other Al-Si Heat-Resistant Aluminum Alloys

Materials Composition (Wt Pct)	Temperature (°C)	UTS (MPa)	Year	Ref.
(2 pct Al_3Zr + 15.2 pct Al_3Ni)/Al-1Mg-0.8Mn-0.8V	350	82	2018	Present study
Al-12Si-3.5Cu-2Mn-1Cr	350	106	2018	10
Al-12Si-0.9Cu-0.8Mg-4Ni	350	116	2017	36
Al-12.5Si-0.84Mg-5Cu-2Ni-0.5Fe-(0.24~0.28) Cr	350	≈92	2015	37
Al-13Si-3Cu-0.6Fe-0.6Mn	340	92	2011	38
Al-13Si-5Cu-0.6Fe-0.6Mn	340	97	2011	38
Al-12.75Si-2.63Cu-1.93Ni	350	78.1	2012	22
Al-12.87Si-5.45Cu-1.83Ni	350	93.5	2012	22
Al-13Si-1.08Cu-1.05Mg-1Ni	350	61.63	2010	21
Al-12.8Si-3.23Cu-1.01Mg-1Ni	350	61.71	2010	21
Al-12.57Si-1.02Cu-1.23Mg-1.07Ni-0.04Mn	350	67.07	2008	39
Al-12.57Si-1.02Cu-1.23Mg-1.07Ni-0.15Mn	350	75.62	2008	39
Al-12.57Si-1.02Cu-1.23Mg-1.07Ni-0.4Mn	350	71.92	2008	39
ZL109 Al-(11~13)Si-(0.5~1.5)Cu-(0.8~1.3)Mg-(0.8~1.5)Ni	350	67.4	2018	10
M124 Al-12Si-1Cu-1Mg-1Ni	350	35 to 55	—	35
M126 Al-16Si-1Cu-1Mg-1Ni	350	35 to 55	—	35
M138 Al-18Si-1Cu-1Mg-1Ni	350	35 to 55	—	35
M244 Al-25Si-1Cu-Mg-1Ni	350	35 to 55	—	35
M142 Al-12Si-3Cu-2Ni-1Mg	350	45 to 65	—	35
M145 Al-15Si-3Cu-2Ni-1Mg	350	45 to 65	—	35
M174 + Al-12Si-4Cu-2Ni-1Mg	350	45 to 65	—	35

ductility of the composites.[26] Therefore, transgranular cleavage fracture of $Al_{10}V$ is also a failure mode of the present composite.

IV. CONCLUSIONS

The as-cast microstructure and tensile properties at room temperature and elevated temperature are studied for in-situ reaction composites (Al_3Zr + Al_3Ni)/Al-1Mg-0.8Mn-0.8V. The main conclusions are summarized as

1. The microstructures of the in-situ composites investigated in the current study are composed of α-Al, Al_3Zr, Al_3Ni, and $Al_{10}V$ phase. The eutectic Al_3Ni phase exhibits lamellar morphology with alternating layers of α-Al. The fine Al_3Zr particles are mainly distributed in the space of Al + Al_3Ni eutectic structure. Some coarse, blocky $Al_{10}V$ phases with low crystal symmetry are scattered in the matrix. Increase in the Al_3Zr content results in the decrease in the size of the primary α-Al dendrites, but the relative amount of Al + Al_3Ni eutectic mixture increases. The Al_3Zr particles tend to agglomerate at greater than 2 wt pct content.
2. The room-temperature tensile strength of the composites increased with the increasing Al_3Ni content. The (2 pct Al_3Zr + 15.2 pct Al_3Ni)/Al-alloy composite shows the best overall mechanical properties, with a tensile strength of 198 MPa and a fracture strain of 6.55 pct. At 200 °C and 300 °C, tensile strengths of composites (2 pct Al_3Zr + 13.3 pct Al_3Ni)/Al-alloy and (2 pct Al_3Zr + 15.2 pct Al_3Ni)/Al-alloy reach 175 MPa and 166 MPa, and 191 MPa and 155 MPa, respectively. At 350 °C, the highest tensile strength reaches 82 MPa, which surpasses some MAHLE Al-Si piston alloys, suggesting its potential application in heat-resistant parts of automotive engines. However, further studies on creep, dynamic properties, and wear behavior would be required before the composite can be used in actual applications.
3. Analysis indicates that the failure mode of the present composites is ductile fracture; the particle strengthening, fiber-reinforced strengthening, and coherent strengthening are the main strengthening mechanisms, while significant eutectic mixture present in the microstructure provides toughening. Transgranular cleavage fracture of coarse, brittle $Al_{10}V$ phase, and the microvoid coalescence fracture are among the main failure mechanisms.

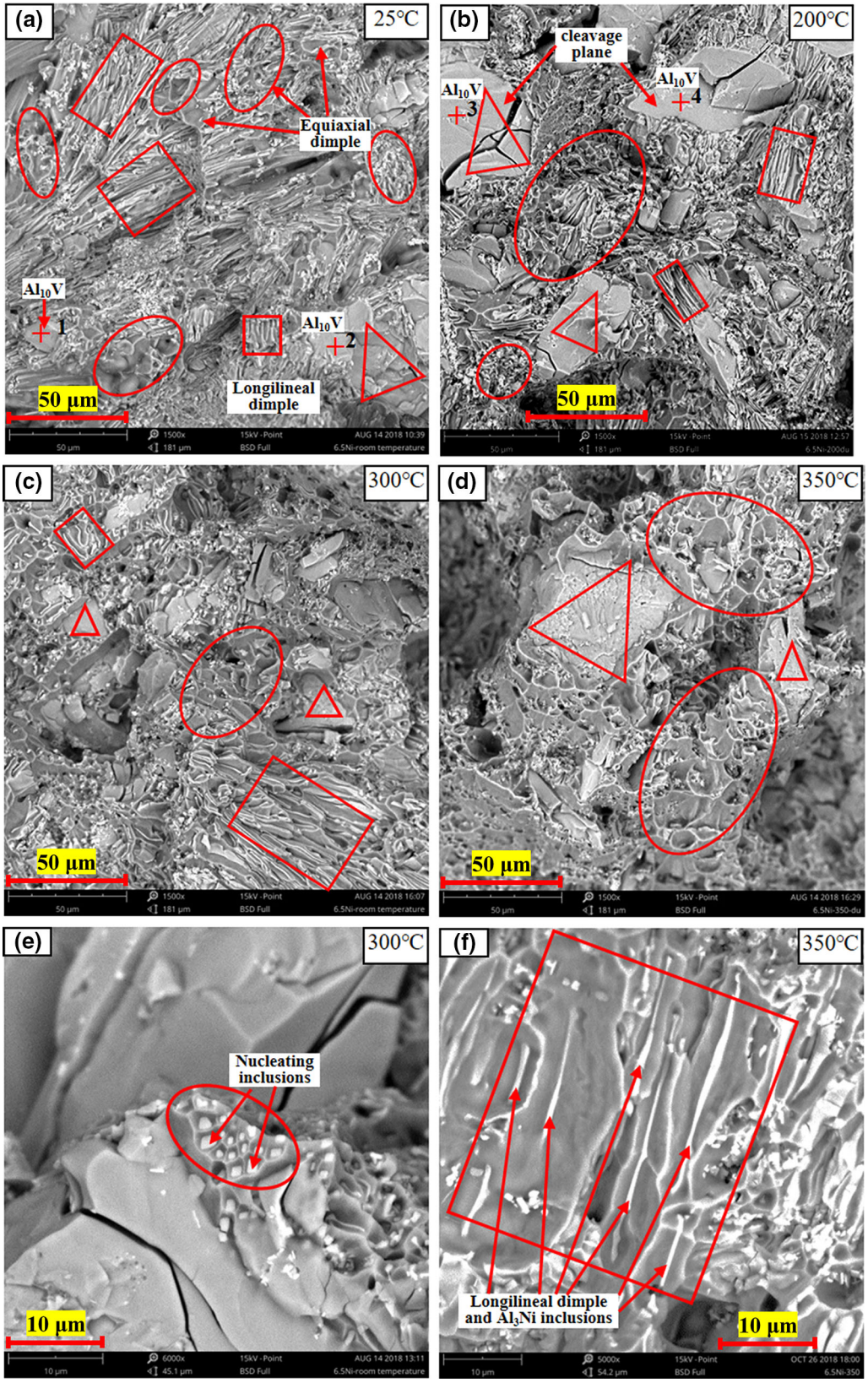

Fig. 10—Microfracture surface morphologies of (2 pct Al_3Zr + 15.2 pct Al_3Ni)/Al-1Mg-0.8Mn-0.8V at different temperatures: (*a*) 25 °C, (*b*) 200 °C, (*c*) 300 °C, (*d*) 350 °C, (*e*) 300 °C at higher magnification, and (*f*) 350 °C at higher magnification.

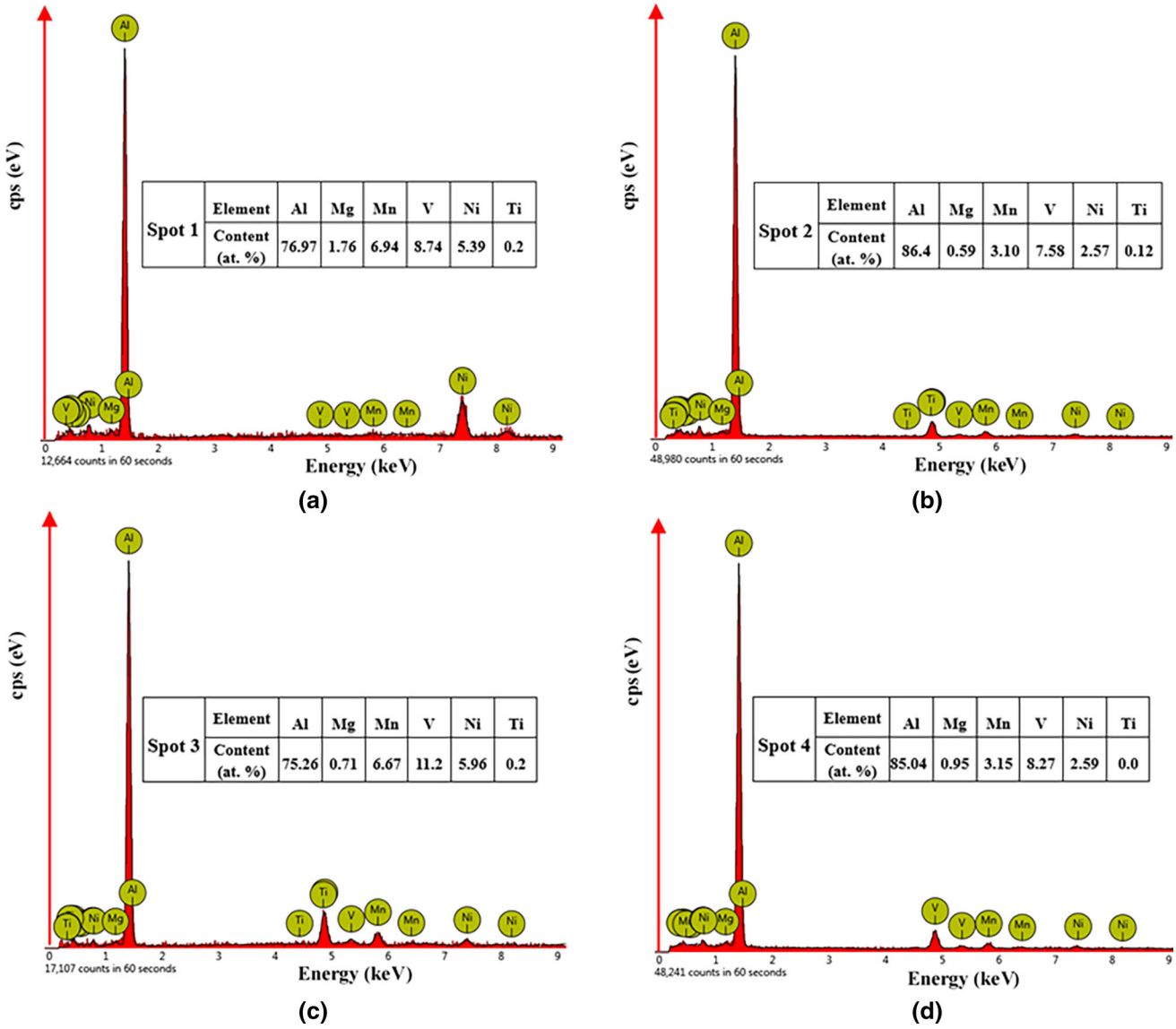

Fig. 11—EDS analysis of Al10V phase in locations shown in Fig. 10(a): (*a*) 1, (*b*) 2 and in Fig. 10(b): (*c*) 3 and (*d*) 4.

ACKNOWLEDGMENTS

The authors acknowledge the supports received from the Guangxi Natural Science Foundation (Grant No. 2016GXNSFAA380223), the Guangxi University Research Fund Project (Grant No. XJZ100343), and the Innovation Drive Development Foundation of Guangxi (Grant No. AA17202011). NG acknowledges the US-Egypt Cooperative Research Project (Award # OISE 1445686). Jieming Wen is thanked for providing the high-temperature electronic universal testing machine for the tensile test.

REFERENCES

1. A.R. Farkoosh, X. Grant Chen, and M. Pekguleryuz: *Mater. Sci. Eng. A*, 2015, vol. 620, pp. 181–89.
2. S. Kumar, R.S. Panwar, and O.P. Pandey: *Metall. Mater. Trans. A*, 2013, vol. 44A, pp. 1548–65.
3. A.B. Pandey, B.S. Majumdar, and D.B. Miracle: *Metall. Mater. Trans. A*, 2000, vol. 31A, pp. 921–36.
4. G. Gautam, A.K. Ghose, and I. Chakrabarty: *Metall. Mater. Trans. A*, 2015, vol. 46A, pp. 5952–61.
5. Z. Asghar, G. Requena, and E. Boller: *Acta Mater.*, 2011, vol. 59 (16), pp. 6420–32.
6. M. Javidani and D. Larouche: *Int. Mater. Rev.*, 2014, vol. 59 (3), pp. 132–58.
7. A.M.A. Mohamed, F.H. Samuel, and S.A. Kahtani: *Mater. Sci. Eng. A*, 2013, vol. 577, pp. 64–72.
8. H. Ye: *J. Mater. Eng. Perform.*, 2003, vol. 12 (3), pp. 288–97.
9. S.K. Shaha, F. Czerwinski, W. Kasprzak, J. Friedman, and D.L. Chen: *Mater. Sci. Eng. A*, 2016, vol. 652, pp. 353–64.
10. G. Li, H. Liao, X. Suo, Y. Tang, U.S. Dixit, and P. Petrov: *Mater. Sci. Eng. A*, 2018, vol. 709, pp. 90–96.
11. J. Rakhmonov, G. Timelli, and F. Bonollo: *Mater. Charact.*, 2017, vol. 128, pp. 100–08.
12. H.M. Lee, J. Lee, and Z.-H. Lee: *Scr. Metall. Mater.*, 1991, vol. 25 (3), pp. 517–20.
13. Y. Fan and M.M. Makhlouf: *Mater. Sci. Eng. A*, 2016, vol. 654, pp. 228–35.

14. J. Rakhmonov, G. Timelli, and F. Bonollo: *Adv. Eng. Mater.*, 2016, vol. 18 (7), pp. 1096–05.
15. K.E. Knipling, D.C. Dunand, and D.N. Seidman: *Z. Metall.*, 2006, vol. 97 (3), pp. 246–65.
16. Y.Y. Fan and M.M. Makhlouf: *Mater. Sci. Forum*, 2013, vol. 765, pp. 8–12.
17. T. Gao, D. Li, Z. Wei, and X. Liu: *Mater. Sci. Eng. A*, 2012, vol. 552, pp. 523–29.
18. J. Hernandez-Sandoval, G.H. Garza-Elizondo, A.M. Samuel, S. Valtiierra, and F.H. Samuel: *Mater. Des.*, 2014, vol. 58, pp. 89–101.
19. J.Y. Uan and T.S. Lui: *Cast. Met.*, 2016, vol. 6 (4), pp. 210–16.
20. M. Ragab and H.G. Salem: *Powder Technol.*, 2012, vol. 222, pp. 108–16.
21. Y. Li, Y. Yang, Y. Wu, L. Wang, and X. Liu: *Mater. Sci. Eng. A*, 2010, vol. 527 (26), pp. 7132–37.
22. Y. Yang, K. Yu, Y. Li, D. Zhao, and X. Liu: *Mater. Des.*, 2012, vol. 33, pp. 220–25.
23. H.N. Girisha and K.V. Sharma: *Int. J. Sci. Eng. Res.*, 2012, vol. 3 (2), pp. 1–4.
24. S.W. Nam and D.H. Lee: *Met. Mater.*, 2000, vol. 6 (1), p. 13.
25. F. Wang, Z. Liu, D. Qiu, J.A. Taylor, M.A. Easton, and M.-X. Zhang: *Acta Mater.*, 2013, vol. 61 (1), pp. 360–70.
26. F. Meng, Z. Wang, Y. Zhao, D. Zhang, and W. Zhang: *Metals*, 2016, vol. 7 (1), p. 10.
27. G. Gautam and A. Mohan: *J. Alloys Compd.*, 2015, vol. 649, pp. 174–83.
28. H.-J. Yang, Y.-T. Zhao, G. Chen, S.-L. Zhang, and D.-B. Chen: *Trans. Nonferrous Met. Soc. China*, 2012, vol. 22 (3), pp. 571–76.
29. J. Lei, W. Xiaolu, L. Hui, Z. Yutao, Y. Yonggang, and C. Jianchao: *Rare Met. Mater. Eng.*, 2016, vol. 45 (11), pp. 2798–2803.
30. H. Wang, G. Li, Y. Zhao, and Z. Zhang: *J. Alloys Compd.*, 2011, vol. 509 (18), pp. 5696–5700.
31. Y. Fan and M.M. Makhlouf: *Metall. Mater. Trans. A*, 2015, vol. 46A, pp. 3808–12.
32. D.R.H. Jones and G.J. May: *Acta Metall.*, 1975, vol. 23, pp. 29–34.
33. J.R. Davies, T.H. Courtney, and M.A. Przystupa: *Metall. Trans. A*, 1980, vol. 11 (2), pp. 323–32.
34. J.Y. Uan, L.H. Chen, and T.S. Lui: *Acta Mater.*, 2001, vol. 49 (2), pp. 313–20.
35. MAHLE GmbH: *Pistons and Engine Testing*, 2nd ed., Springer, Stuttgart, 2016.
36. J. Feng, B. Ye, L. Zuo, R. Qi, Q. Wang, H. Jiang, R. Huang, and W. Ding: *Mater. Sci. Eng. A*, 2017, vol. 706, pp. 27–37.
37. Y. Yang, S.-Y. Zhong, Z. Chen, M. Wang, N. Ma, and H. Wang: *J. Alloys Compd.*, 2015, vol. 647, pp. 63–69.
38. E.R. Wang, X.D. Hui, and G.L. Chen: *Mater. Des.*, 2011, vol. 32 (8–9), pp. 4333–40.
39. Z. Qian, X. Liu, D. Zhao, and G. Zhang: *Mater. Lett.*, 2008, vol. 62 (14), pp. 2146–49.
40. T. Hatano: *Phys. Rev. B*, 2006, vol. 74 (2), p. 020102(R).
41. X. Wang, Y. Zhao, G. Chen, X. Cheng, H. Zhang, and Z. Zhang: *Rare Met. Mater. Eng.*, 2007, vol. 36 (2), pp. 259–63.
42. K. Yamashita, I. Fujimoto, T. Murakumo, S. Kumal, and A. Sato: *Philos. Mag. A*, 2000, vol. 80 (1), pp. 219–35.
43. G. Peng, Z. Tietao, X. Xiaoqing, G. Zhi, and C. Li: *Rare Met. Mater. Eng.*, 2013, vol. 42 (1), pp. 6–13.